Tellus (1992), *44A*, 197–216

A three-dimensional large-scale cloud model: testing the role of radiative heating and ice phase processes

By J. L. LEE, K. N. LIOU and S. C. OU, *Department of Meteorology/CARSS, University of Utah, Salt Lake City, Utah 84112, USA*

(Manuscript received 23 September 1991; in final form 7 January 1992)

ABSTRACT

A time-dependent, three-dimensional, large-scale cloud model has been developed for the prediction of cloud cover, cloud liquid/ice water content (LWC/IWC), precipitation, specific humidity and temperature. Partial cloudiness is allowed to form when large-scale relative humidity is less than 100%. Both liquid and ice phases are included in the model. The liquid phase processes consist of evaporation, condensation, autoconversion and precipitation. The ice phase processes include heterogeneous nucleation to generate ice crystals, depositional growth to simulate Bergeron-Findeisen's process, sublimation to deplete ice crystals, and gravitational settling of ice crystals. The radiative transfer parameterization scheme is based on a broadband method and involves the transfer of infrared and solar radiation in clear and cloudy regions. The broadband infrared emissivity, reflectivity, and transmissivity for cirrus clouds, as well as the broadband solar absorption, reflection, and transmission values for low, middle and high clouds are computed based on the cloud LWC and IWC interactively generated by the cloud model. Large amounts of satellite data, including cloud cover climatology derived from the US Air Force three-dimensional nephanalysis (3DNEPH) and earth radiation budget (ERB), have been processed into formats appropriate for verification. The 96-h model simulations of cloud cover, outgoing long-wave radiation (OLR), and cloud LWC have been verified against data analyzed from 3DNEPH, ERB and the Nimbus-7 Scanning Multichannel Microwave Radiometer (SMMR) satellite observations, respectively. The predicted cloud IWC is compared to in situ observations as well as to results from other studies. The predicted cloud and radiation results compare well with those analyzed from satellite data. Numerical experiments are carried out with and without radiative heating and ice phase processes in the cloud formation scheme. The inclusion of radiative heating produces a significant change in temperature, cloud cover and total cloud water content, while the inclusion of ice phase processes generates a substantial change only in total cloud water content. If the cloud LWC is sufficiently large to initiate effective Bergeron-Findeisen's processes, the total cloud water content decreases, indicating that gravitational settling is an efficient mechanism in reducing the cloud IWC.

1. Introduction

Clouds regularly occupy about 50% of the sky. They are the most important regulators of the earth's radiation budget, i.e., the balance between net solar radiation and outgoing longwave radiation at the top of the atmosphere (TOA), by which the earth's climate is determined. On the one hand, clouds reflect a large portion of incoming solar radiation, producing a cooling effect referred to as the solar albedo effect. On the other, they trap the outgoing longwave radiation emitted from the earth, resulting in a warming effect referred to as the IR greenhouse effect. Since the greenhouse and albedo effects are different in sign as well as magnitude, the existence of clouds may have a profound impact upon the sensitivity of climate to external perturbations, such as the increase of atmospheric carbon dioxide. In particular, cirrus clouds, which regularly cover about 20% of the globe, are optically thin and nonblack. The outcome of the greenhouse-versus-albedo effects is intrinsically modified by the radiative effects of nonblack cirrus (Liou, 1986).

Recognizing the importance of clouds in weather and climate processes, numerous

modeling efforts have been carried out to understand the relative significance of solar albedo and IR greenhouse effects involving clouds. In early models, the formation of clouds was very crude and lacked physical foundation. An arbitrary fractional amount of cloud was assigned to a given layer where large-scale condensation occurs. All the excessive water vapor was condensed and immediately precipitated onto the ground. As a result, there was no cloud water or cloud ice remaining in the clouds. These two elements are necessary for the calculation of cloud radiative effects. In climatic perturbation studies, Wetherald and Manabe (1988) assigned a cloud amount of 80% to condensation and found that cloud feedback processes enhance the sensitivity of the model climate to an increase in atmospheric carbon dioxide. This conclusion is in agreement with that drawn by Hansen et al. (1983). The features of cloud cover change obtained in these studies, as well as in that of Washington and Meehl (1984), are qualitatively similar.

Efforts have also been focused on improving the specification of the radiative properties of clouds and cloud parameterization schemes in GCMs to demonstrate the importance of cloud-radiation interaction to the simulation of atmospheric circulation. Ramanathan et al. (1983) demonstrated that refinement in radiative properties of nonblack high cirrus emissivity significantly improves the model simulation of atmospheric temperatures as well as that of zonal mean winds. Slingo and Slingo (1988) reached the same conclusion in their study of cloud longwave radiative forcing. Using a GCM designed for medium range weather prediction, Liou and Zheng (1984) illustrated the importance of cloud and radiative processes to the maintenance of the Hadley circulation.

In order to incorporate interactive cloud and radiation processes in models, cloud liquid water content (LWC) and ice water content (IWC) are required for radiation calculations. The models must be able to generate LWC/IWC. This is the so-called prognostic method, which requires the additional prognostic equation(s) for the prediction of LWC/IWC. Sundqvist (1978) made the first attempt to develop a physically based prognostic large-scale cloud scheme for use in a GCM. In his approach, the cloud LWC is a prognostic variable determined by various source and sink terms which are parameterized in terms of associated bulk quantities. Also partial cloudiness is allowed to exist when the large-scale relative humidity is less than 100%. Sundqvist (1981) incorporated the proposed cloud scheme into the European Centre for Medium Range Weather Forecasts (ECMWF) model and carried out a 5-day integration. The forecast and cloud amounts were compared with satellite photographs, which showed that the cloud patterns are reasonably well-simulated; the predicted cloud LWC is within the observational range. However, these studies did not include radiative effects and ice phase processes. The importance of including a more realistic and physically based parameterization for cloud parameters in GCMs has recently been articulated by Sundqvist (1988).

Mitchell et al. (1989) conducted a study of cloud feedback in the UK Meteorological Office GCM. A cloud liquid water budget equation was included in the model. However, ice clouds were not generated from the budget equation. Water cloud radiative properties are interactive in the model based on the schemes developed by Liou and Wittman (1979) for solar radiation and Stephens (1978) for IR radiation. Roeckner (1988) also included a water budget equation in the University of Hamburg GCM to undertake a study of the feedback processes involving clouds due to external radiative forcing. Smith (1990) incorporated a prognostic cloud water budget equation in a GCM and compared the simulated cloud and radiation fields with satellite observations.

Interactive cloud formation in a model setting would require a detailed consideration of the sources and sinks of water and ice particles. The inclusion of separate empirical equations for cloud LWC (e.g., Xu and Krueger, 1991), IWC (e.g., Heymsfield and Donner, 1990) and precipitation in the GCM (i.e., diagnostic approach) would appear to be extremely difficult and inconsistent with respect to the model physics. In order to understand the role of radiative heating and ice phase processes in the formation of large-scale clouds, we have developed a global stratiform cloud model that includes prognostic cloud LWC, IWC and precipitation equations as well as an interactive radiative transfer program. The wind fields required for the simulation are determined from a GCM. In Section 2, we describe a large-scale cloud model and an interactive radiation program. Section 3 contains bulk parameteriza-

tions of various sources and sinks for the cloud microphysical processes simulated in the model. Section 4 presents comparisons of model predictions and verification data, including a description of model input and verification data. Results on the numerical experiments on atmospheric radiation and ice phase processes are shown in Section 5. Finally, conclusions are given in Section 6.

2. Model description

2.1. Governing equations

We have developed a time-dependent, three-dimensional cloud-moisture model for the prediction of water vapor, cloud LWC, cloud IWC, precipitation and temperature. The first four variables are governed by the law of mass conservation. The latent heat exchanges during the phase transitions of water substances are determined by the first law of thermodynamics through the temperature field. The governing equations may be written as follows:

$$\frac{\partial}{\partial t}(\bar{\rho}\bar{T})+\frac{1}{a\cos\phi}\left[\frac{\partial}{\partial\lambda}(\bar{\rho}\bar{T}\bar{u})+\frac{\partial}{\partial\phi}(\bar{\rho}\bar{T}\bar{v}\cos\phi)\right]+\frac{\partial}{\partial z}(\bar{\rho}\bar{T}\bar{w})+\bar{\rho}\Gamma_{\mathrm{d}}\bar{w}=\bar{\rho}(\bar{Q}_{\mathrm{c}}+\bar{Q}_{\mathrm{R}})-\frac{L_{\mathrm{c}}}{C_{\mathrm{p}}}\bar{E}_{\mathrm{r}}+\frac{L_{\mathrm{f}}}{C_{\mathrm{p}}}\bar{S}_{\mathrm{BF}}-\frac{L_{\mathrm{d}}}{C_{\mathrm{p}}}\bar{S}_{\mathrm{s}}+F_{\mathrm{H}}^{\mathrm{T}}+F_{\mathrm{V}}^{\mathrm{T}},\tag{2.1}$$

$$\frac{\partial}{\partial t}(\bar{\rho}\bar{q}_{\mathrm{v}})+\frac{1}{a\cos\phi}\left[\frac{a}{a\lambda}(\bar{\rho}\bar{q}_{\mathrm{v}}\bar{u})+\frac{\partial}{\partial\phi}(\bar{\rho}\bar{q}_{\mathrm{v}}\bar{v}\cos\phi)\right]+\frac{\partial}{\partial z}(\bar{\rho}\bar{q}_{\mathrm{v}}\bar{w})=-\frac{C_{\mathrm{p}}}{L_{\mathrm{c}}}\bar{\rho}\bar{Q}_{\mathrm{c}}+\bar{\rho}\bar{E}_{\mathrm{r}}+\bar{S}_{\mathrm{s}}+F_{\mathrm{H}}^{q_{\mathrm{v}}}+F_{\mathrm{V}}^{q_{\mathrm{v}}},\tag{2.2}$$

$$\frac{\partial}{\partial t}(\bar{\rho}\bar{q}_{\mathrm{l}})+\frac{1}{a\cos\phi}\left[\frac{\partial}{\partial\lambda}(\bar{\rho}\bar{q}_{\mathrm{l}}\bar{u})+\frac{\partial}{\partial\phi}(\bar{\rho}\bar{q}_{\mathrm{l}}\bar{v}\cos\phi)\right]+\frac{\partial}{\partial z}[\bar{\rho}\bar{q}_{\mathrm{l}}(\bar{w}-\bar{w}_{\mathrm{l}})]=\frac{C_{\mathrm{p}}}{L_{\mathrm{c}}}\bar{\rho}\bar{Q}_{\mathrm{c}}-\bar{\rho}\bar{P}-\bar{S}_{\mathrm{BF}}+F_{\mathrm{H}}^{q_{\mathrm{l}}}+F_{\mathrm{V}}^{q_{\mathrm{l}}},\tag{2.3}$$

$$\frac{\partial}{\partial t}(\bar{\rho}\bar{q}_{\mathrm{i}})+\frac{1}{a\cos\phi}\left[\frac{\partial}{\partial\lambda}(\bar{\rho}\bar{q}_{\mathrm{i}}\bar{u})+\frac{\partial}{\partial\phi}(\bar{\rho}\bar{q}_{\mathrm{i}}\bar{v}\cos\phi)\right]+\frac{\partial}{\partial z}[\bar{\rho}\bar{q}_{\mathrm{i}}(\bar{w}-\bar{V}_{\mathrm{T}})]=\frac{C_{\mathrm{p}}}{L_{\mathrm{d}}}\bar{\rho}\bar{Q}_{\mathrm{i}}+\bar{S}_{\mathrm{BF}}-\bar{S}_{\mathrm{s}}+F_{\mathrm{H}}^{q_{\mathrm{i}}}+F_{\mathrm{V}}^{q_{\mathrm{i}}},\tag{2.4}$$

$$-\frac{\partial}{\partial z}(\tilde{P})=\bar{\rho}\bar{P}-\bar{\rho}\bar{E}_{\mathrm{r}}.\tag{2.5}$$

In these equations, an overbar denotes the average of a variable over a grid space. The variables $\bar{u}$, $\bar{v}$, and $\bar{w}$ are wind fields and are obtained from a GCM; λ and ϕ are the longitude and latitude, respectively; $\bar{\rho}$ is the air density, $\bar{T}$ the temperature, C_{p} the specific heat at constant pressure, Γ_{d} the adiabatic lapse rate, $\tilde{P}$ the precipitation flux, $\bar{q}_{\mathrm{v}}$, $\bar{q}_{\mathrm{l}}$, $\bar{q}_{\mathrm{i}}$ the mixing ratios for water vapor, cloud water, and cloud ice, respectively, and L_{c}, L_{d} and L_{f} the latent heat of condensation, sublimation, and melting, respectively. Also in these equations, $\bar{Q}_{\mathrm{c}}$, $\bar{Q}_{\mathrm{i}}$ and $\bar{Q}_{\mathrm{R}}$ represent the condensational heating rates for cloud water, cloud ice, and the radiative heating rate, respectively, $\bar{P}$ is the rate of autoconversion from cloud droplets to raindrops, $\bar{E}_{\mathrm{r}}$ is the evaporation of rain water, $\bar{S}_{\mathrm{BF}}$ and $\bar{S}_{\mathrm{s}}$ are the rates of change of the mass of ice particles due to Bergeron-Findeisen's process and sublimation, respectively, and $\bar{w}_{\mathrm{l}}$ and $\bar{V}_{\mathrm{T}}$ are the bulk terminal velocities for cloud water and ice particles, respectively. The total precipitation including rain and snow in a unit area at the surface for a given time period Δt is given by: $-\Delta t[\tilde{P}+\bar{\rho}q_{\mathrm{i}}(\bar{w}-\bar{V}_{\mathrm{T}})]/\bar{\rho}_{\ell}$, where $\bar{\rho}_{\ell}$ is the liquid water density. In addition, the vertical eddy flux and horizontal diffusion terms have been denoted by F_{V}^{χ} and F_{H}^{χ}, respectively, where χ can be $\bar{T}$, $\bar{q}_{\mathrm{v}}$, $\bar{q}_{\mathrm{l}}$ or $\bar{q}_{\mathrm{i}}$.

The cloud cover, η, is derived based on an average of the specific humidities over clear and cloudy regions in the form

$$\bar{q}=\eta q_{\mathrm{c}}+(1-\eta)\,q_0,\tag{2.6}$$

where q_{c} and q_0 are, respectively, the specific humidity in the cloudy and clear regions. After rearranging terms, the cloud cover is given by

$$\eta=\frac{\bar{q}_{\mathrm{v}}/\bar{q}_{\mathrm{s}}-q_0/\bar{q}_{\mathrm{s}}}{q_{\mathrm{c}}/\bar{q}_{\mathrm{s}}-q_0/\bar{q}_{\mathrm{s}}}.\tag{2.7}$$

Here, we have introduced the grid-averaged saturation specific humidity, $\bar{q}_s(\bar{T})$, which is a function of the grid-averaged temperature, $\bar{T}$. For a stratiform cloud, the temperature within the cloud is approximately equal to the grid-averaged temperature, i.e., $q_c \approx \bar{q}_s(\bar{T})$. Thus,

$$\eta \approx \frac{(\bar{h}-h_0)}{(1-h_0)}, \tag{2.8}$$

where $\bar{h}=\bar{q}_v/\bar{q}_s$ is the averaged relative humidity and $h_0=q_0/\bar{q}_s$ is referred to as the threshold relative humidity, which is a parameter to be prescribed to close the model equations.

The cloud cover expression in eq. (2.8) denotes a linear relation between the relative humidity and cloud cover. A similar empirical relation based on observations has been developed by Smagorinsky (1960) for use in GCMs (Fig. 1). For the present large-scale studies we have used the threshold relative humidity presented in Fig. 1 for the calculation of high, middle and low cloud covers.

With the introduction of the threshold relative humidity ($h_0<1$), partial cloudiness in the grid box is allowed when the large-scale relative humidity is less than 100%. The cloudy area and clear region in a grid box are denoted by η and $(1-\eta)$, respectively. Condensation occurs in the cloudy area; evaporation takes place in the clear region. Raindrops formed in a given layer are not subject to evaporation whithin that layer. Instead, raindrops that fall through this layer from higher clouds may evaporate in the clear region of the layer.

Since the averaged terminal velocity of cloud droplets is on the order of 1 cm/s, which is close to the large scale vertical velocity, we would expect that the terminal velocity of cloud droplets and vertical air motion roughly cancel each other in stratiform clouds. Therefore, vertical advection of cloud LWC in eq. (2.3) is omitted in the model calculations. The vertical eddy fluxes are calculated from a K-theory approach (Liou and Ou, 1983) and the diffusion terms in spherical coordinates are parameterized based on the methodology described by Washington and Williamson (1977). Because clouds are allowed to form only above the 0.925 σ-level, the turbulent fluxes involving clouds are not computed at the surface.

2.2. *Cloud microphysical processes*

The cloud microphysical processes simulated in the present cloud model are illustrated in Fig. 2. Both the liquid and ice phase processes are included, with the liquid phase on the left-hand side and ice phase on the right-hand side of the diagram. The liquid phase processes consist of condensation of water vapor into cloud liquid water at temperatures warmer than $-40°C$, conversion of cloud liquid water into rain water by means of autoconversion, and precipitation of rain water onto the ground. Evaporation of cloud and rain water increases the specific humidity.

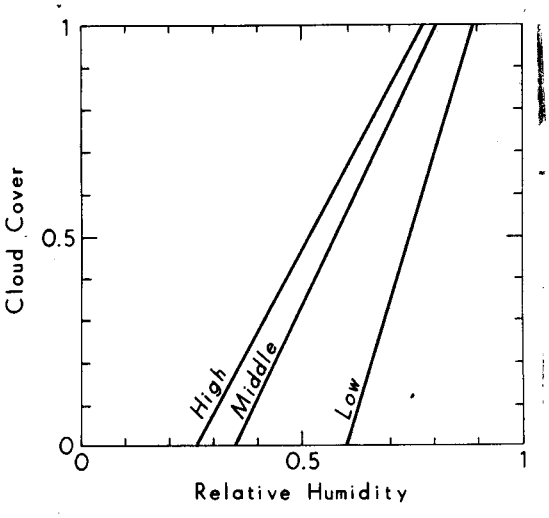

Fig. 1. Empirical relations between the low-, middle-, and high-cloud amount and relative humidity (Smagorinsky, 1960). The values of h_0 for low, middle, and high clouds are 0.6, 0.35, and 0.26, respectively.

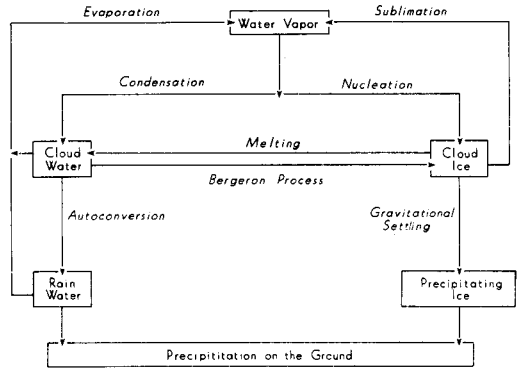

Fig. 2. Schematic display of the cloud microphysical processes simulated in the model.

The ice phase processes include both heterogeneous and homogeneous nucleations of water condensate to form cloud ice. Homogeneous nucleation occurs at temperatures colder than −40°C. Cloud ice is converted to precipitation ice by virtue of gravitational settling, in which the downward ice flux is calculated by integrating the mass and fall velocity of an individual ice crystal over the whole spectrum of ice crystals. The sublimation of cloud ice increases the specific humidity. At temperatures above the freezing point, the melting process converts cloud ice to cloud water.

An important link between the liquid and ice phases is the so-called Bergeron-Findeisen process. The saturation vapor pressure over ice is less than that over water. As a result, ice crystals grow by diffusion at the expense of the supercooled liquid cloud droplets. Once generated by ice nucleation, ice crystals grow by deposition due to Bergeron-Findeisen's process and are depleted by sublimation as well as the gravitational settling. Above the freezing point, clouds consist entirely of cloud water. In the region 0° to −40°C, cloud water and cloud ice may coexist. At temperatures below −40°C, cloud ice dominates because of homogeneous nucleation.

The formation of rimed crystals, such as graupel and hail, is not considered in this model since they occur more frequently in convective clouds than in large-scale stratiform clouds.

2.3. *Numerical implementation*

In the horizontal, the grid point space is characterized by 48 equally-spaced longitudinal points and 38 Gaussian latitudes, which is the same as the horizontal grid structures used in the Air Force Geophysics Laboratory (AFGL) GCM (Yang et al., 1989). We have used this model to provide the present cloud model with initial data and a wind field. The horizontal grid space in the model has been modified near the poles to maintain nearly constant geographical distances between the grid points. In the vertical, a 16-layer stretched z-coordinates is used in the cloud model.

The upstream scheme is utilized as a means of numerically differencing the horizontal and vertical advection terms. The scheme is conditionally stable and its stability criterion follows the Courant-Friedrichs-Levy (CFL) condition, i.e., $C_{max}\,\Delta t/\Delta S < 1$, where C_{max} is the maximum velocity in the computational domain, Δt is the time step and ΔS is the grid size. This criterion is easily satisfied in large scale models. For example, in the vertical where $\bar{w}_{max} \sim 10^0$ cm/s, $\Delta t \sim 10^3$, and $\Delta S \sim 10^5$ cm, the criterion is much less than 1. The time step used in this study is 30 minutes. We have carried out an experiment to investigate the required time step for radiation calculations. The results produced by using 30-min or 3-h time steps are practically the same. For this reason, the radiation calculations are updated every 3 h, i.e., the radiative heating rates are calculated every 3 hours at every horizontal grid point.

2.4. *Radiative transfer parameterization*

The radiative transfer parameterization program used in this study is based on a broadband method and involves the transfer of thermal IR and solar radiation in clear and cloudy regions. In a clear atmosphere, the entire IR spectrum is divided into five bands: three for H_2O, one for CO_2, and one for O_3 absorption. The parameterizations of these broadband IR emissivities, which included H_2O and CO_2 overlap, were developed by Liou and Ou (1981) and Ou and Liou (1983). The solar spectrum consists of 25 bands: 6 for H_2O, 1 for CO_2, which overlaps the H_2O 2.7-μm band, and 18 for O_3.

In a cloudy atmosphere, low and middle clouds are treated as blackbodies in the IR radiative transfer calculation. The broadband IR emissivity, reflectivity, and transmissivity for high clouds, as well as the broadband solar absorption, reflection, and transmission values for low, middle, and high clouds, were computed based on the cloud LWC and IWC interactively generated by the cloud model. The cloud radiative properties were calculated, based on the parameterizations developed by Liou and Wittman (1979). Accuracy of all the aforementioned parameterization was verified via more comprehensive and exact radiative transfer calculations described by Ou and Liou (1988). In the parameterization, there are upper and lower limits for cloud LWP. For low clouds, for example, the limits are 600 and 40 g m^{-2}. In unusual circumstances where the predicted LWPs are larger or smaller than the preset limits, these preset values are used in the calculation of the solar radiative properties.

The radiative heating rate at level z is related to the divergence of the net fluxes and is given by

$$\frac{\partial \bar{T}}{\partial t} = -\frac{1}{\bar{\rho} C_p} (\Delta F/\Delta z), \tag{2.9}$$

where Δz is the model layer thickness and ΔF is the net radiative flux difference between the layer top and bottom. This equation applies to both IR and solar heating rate calculations with downward solar flux and upward IR flux defined as positive. For the transfer of solar radiation in a cloud layer, the net flux density decreases from the cloud top to the bottom because of cloud absorption and scattering. The absorbed radiant energy leads to the heating of the cloud layer. For black clouds (low or middle clouds), the IR radiative flux is proportional to the fourth power of the absolute temperature of the cloud. Since the atmospheric temperature usually decreases with height, the downward IR flux emitted by the atmosphere above a black cloud top is much smaller than that emitted upward by the black cloud. As a result, the net flux near the cloud top is greater than zero and leads to strong IR cooling in the region. Similarly, there is IR heating near the cloud bottom.

Specification of the overlap that occurs between cloud layers is required for the calculation of radiative transfer in a radiation model. In this study, the model-generated clouds are strapped into three cloud decks. Low, middle, and high clouds fill, respectively, layers (4, 5, 6), layers (7, 8), and layers (9, 10). The cloud cover for each deck of clouds is obtained by averaging model cloud covers as follows:

$$\eta_\ell = (\eta_4 + \eta_5 + \eta_6)/3, \tag{2.10a}$$

$$\eta_m = (\eta_7 + \eta_8)/2, \tag{2.10b}$$

$$\eta_h = (\eta_9 + \eta_{10})/2, \tag{2.10c}$$

where η_ℓ, η_m and η_h denote deck cloud covers for low, middle, and high clouds, respectively.

To determine the total cloud amount, we have assumed that clouds overlap each other in a statistically random manner. Thus the total cloud cover is given by

$$\eta = 1 - (1-\eta_\ell)(1-\eta_m)(1-\eta_h), \tag{2.11}$$

where η is the total cloud cover over a grid area. We have also used maximum overlap scheme in the total cloud cover calculation. However, this scheme produces cloud cover results that significantly underestimate the observed values.

For partly cloudy conditions, the radiative heating/cooling rate at each model layer is obtained by linearly weighting the percentages of the total cloud cover, η, and clear portion, $(1-\eta)$, in the form

$$\left(\frac{\partial \bar{T}}{\partial t}\right)^{pc} = \eta \left(\frac{\partial \bar{T}}{\partial t}\right)^{c} + (1-\eta)\left(\frac{\partial \bar{T}}{\partial t}\right)^{nc}, \tag{2.12}$$

where the superscripts ^{pc}, ^{c}, and ^{nc} represent partly cloudy, cloudy, and clear conditions, respectively.

3. Bulk parameterization of cloud microphysics

Since it is not practical in a large-scale cloud model to simulate detailed microphysical processes with respect to each individual cloud particle, we must relate these processes in terms of bulk quantities, which represent the various sources and sinks for cloud water substances.

3.1. Liquid phase

3.1.1. Condensation. In principle, condensation may be evaluated on the basis of microphysical cloud processes. However, for application to large-scale processes, clouds must be allowed to form in a grid box when the model relative humidity is much less than 1. For this reason, we have used the following scheme to compute condensation. Condensation occurs as a result of expanding air under saturation conditions and may be related to the time rate of change of the saturation vapor pressure. Consequently, the condensational heating rate may be derived from the first law of thermodynamics, the Clausius-Clapeyron equation and the hydrostatic approximation as follows:

$$\bar{Q}_c = \eta \Gamma_d \frac{\bar{q}_s(\bar{T})}{R_a} \left(\frac{L R_a - C_p R_v \bar{T}}{C_p R_v \bar{T}^2 + \bar{q}_s L^2}\right) \bar{w}, \tag{3.1}$$

where Γ_d is the dry adiabatic lapse rate, R_a is the gas constant for air, R_v is the gas constant for water vapor, L is the latent heat for liquid and vapor phases, and $\bar{q}_s$ is the saturation vapor

pressure. The condensation is strongly dependent on the vertical velocity, $\bar{w}$. As saturated air rises, i.e., $\bar{w}>0$, condensation takes place and cloud forms, while depletion of clouds occurs with descending saturated air. The present scheme differs from that developed by Sundqvist (1978) in that condensation and evaporation are computed explicitly.

3.1.2. Autoconversion. Autoconversion is a process through which small cloud droplets merge into large raindrops. The parameterization of autoconversion follows the simple exponential form developed by Sundqvist (1978):

$$\bar{P}=c_0\bar{q}_l\{1-\exp[-(\bar{q}_l/(\eta q_{lr}))^2]\}, \tag{3.2}$$

where c_0 denotes the typical time for the conversion of droplets to raindrops, and q_{lr} is a reference value of cloud LWC above which the conversion from cloud droplets to raindrops increases rapidly. These two values function in a manner similar to the rate of conversion and the accretion parameterization developed by Kessler (1969). We find that Sundqvist's and Kessler's parameterizations produce about the same results for the normal range of cloud LWC. Eq. (3.2) has been used in this study for its simplicity in large-scale cloud modeling.

3.1.3. Evaporation of raindrops. The evaporation of raindrops may be derived from the combination of the Fick law of mass diffusion and the Marshall-Palmer raindrop size distribution. The size distribution is assumed to remain the same throughout the whole process of evaporation. The raindrop evaporation rate is given by

$$\bar{E}_r=K_e(1-\bar{h})\,\bar{P}^{0.42}, \tag{3.3}$$

where the evaporation rate constant K_e is $1.785\times10^{-2}\bar{q}_s$.

3.2. Ice phase

The ice phase parameterizations include homogeneous/heterogeneous nucleation to generate ice crystals, depositional growth to simulate the Bergeron-Findeisen process, sublimation and melting of ice crystals, and gravitational settling to deplete the ice crystals. The Bergeron-Findeisen process occurs primarily at temperatures between 0° and −40°C, while below −40°C homogeneous nucleation dominates. The parameterizations of these source and sink terms are described below.

3.2.1. Homogeneous nucleation. Homogeneous nucleation takes place whenever condensation occurs at temperatures below −40°C. Homogeneous nucleation is analogous to the liquid water condensation process, and may be written in the form:

$$\bar{Q}_i=\eta\Gamma_d\frac{\bar{q}_s(\bar{T})}{R_a}\left(\frac{L_dR_a-C_pR_v\bar{T}}{C_pR_v\bar{T}^2+\bar{q}_sL_f^2}\right)\bar{w}, \tag{3.4}$$

where L_d is the latent heat for ice and vapor phases.

3.2.2. Heterogeneous nucleation. Heterogeneous nucleation leads to the formation of ice crystals on active ice nuclei primarily at temperatures between 0° and −40°C. Based on the experimental work of Mason (1971) and Koenig and Murray (1976), it is assumed that the active ice-forming nuclei (IN) concentration may be expressed in terms of temperature as follows:

$$N=A_1\exp\left\{-\frac{\ln(10)}{A_2}\max[(T-T_0),T^*]\right\}, \tag{3.5}$$

where $A_1=1$, $A_2=4$, $T^*=0$°C, and T_0 is a threshold temperature, which is taken to be −20°C. Here, it is assumed that when the saturated air temperature is lower than T_0, the total number of IN remains the same as that at T_0.

The heterogenous nucleation rate of ice crystals, S_h, is given by

$$S_h=m_0\frac{dN}{dt}, \tag{3.6}$$

where m_0 is the mass of a newly nucleated ice crystal, prescribed as 10^{-11} g, which is equivalent to an ice sphere with a diameter of 2.77 μm (Koenig and Murray, 1976), and

$$\frac{dN}{dt}=\begin{cases}\dfrac{N_{t+\Delta t}-N_t}{\Delta t} & \text{if } T\geqslant-20\text{°C}\\ 0 & \text{if } T<-20\text{°C}.\end{cases} \tag{3.7}$$

Here, $N_{t+\Delta t}$ and N_t are the IN concentrations at consecutive time steps of $t+\Delta t$ and t, respectively.

3.2.3. Bergeron-Findeisen process. The Bergeron-Findeisen process transforms cloud water into cloud ice at temperatures between 0° and −40°C.

To simplify the complicated vapor diffusion equation, Koenig (1971) developed a simple equation to describe the crystal vapor diffusion growth rate as a function of mass. The equation is written as follows:

$$\frac{dm}{dt} = a_3 m^{a_4}, \tag{3.8}$$

where a_3 and a_4 are temperature-dependent parameters given in Koenig (1971), and m is the crystal mass in grams.

The bulk quantity of the ice crystal depositional rate, denoted as S_{BF}, may be derived from eq. (3.8) by multiplying both sides by N, as follows:

$$\bar{S}_{BF} = \frac{d}{dt}(\bar{\rho}\bar{q}_i) = \eta f_1 N^{1-a_4} a_3 (\bar{\rho}\bar{q}_i)^{a_4}, \tag{3.9}$$

where $f_1 = \bar{q}_l/(\bar{q}_l + \bar{q}_i)$ is the cloud liquid fraction serving as an adjustment factor, which allows for higher ice crystal growth rates with more cloud water. The growth is terminated if there is no cloud water to supply water vapor.

3.2.4. Sublimation and melting of ice crystals. Similar to the derivation for the evaporation of raindrops, we have developed the following equation for the rate of sublimation:

$$\bar{S}_s = 0.1037(\bar{\rho}\bar{q}_s)(1-\bar{h})(\bar{\rho}\bar{q}_i)^{0.65}. \tag{3.10}$$

At temperatures above 0°C, cloud ice crystals are assumed to melt instantaneously.

3.2.5. Gravitational settling. Gravitational settling is an important sink for cloud IWC. Therefore, it is desirable to have a representative (mean-volume-weighted) downward flux of ice water. Following Starr and Cox (1985), the downward ice flux may be expressed as:

$$\bar{V}_T(\bar{\rho}\bar{q}_i) = \int_{L_{min}}^{L_{max}} nmv \, dL, \tag{3.11}$$

where n, m, and v are the ice crystal size distribution, mass and terminal velocity of an ice crystal, respectively, and L is the maximum dimension of an ice crystal. L_{min} and L_{max} are the minimum and maximum sizes of ice crystals. The cloud IWC may be further related to n and m as

$$\bar{\rho}\bar{q}_i = \int_{L_{min}}^{L_{max}} nm \, dL. \tag{3.12}$$

In order to calculate the downward ice flux, the size distribution, mass, and terminal velocity for the precipitating ice crystals need to be specifically expressed in terms of the maximum dimension of ice crystals.

The size distributions of ice crystals in mid-latitude cirrus clouds have been measured from aircraft using an optical probe (Heymsfield, 1977). Using these data, Heymsfield and Platt (1984) have averaged all spectra of crystals within every 5°C temperature interval ranging from −20°C to −60°C. The ice crystal size distributions in terms of the maximum dimension of ice crystals may then be parameterized for different temperature ranges in the form

$$n = a_n L^{b_n}, \tag{3.13}$$

where a_n and b_n are temperature dependent empirical coefficients.

The minimum length that the optical probe can measure is about 20 μm. Small ice crystals less than 20 μm in size could be missed by the measurement technique. Consequently, small ice crystal data were excluded from the analysis by Heymsfield and Platt (1984). For this reason, 20 μm is taken as the minimum length of ice crystals, L_{min}, which is needed in the calculations of Eqs. (3.11) and (3.12).

3.2.6. Crystal mass and terminal velocity. The individual ice crystal mass, m, may be parameterized in terms of the maximum dimension of an ice crystal, L, as follows:

$$m = a_m L^{b_m}, \tag{3.14}$$

where m and L are in units of grams and μm, respectively. The constants a_m and b_m associated with various ice crystal habits are given in Heymsfield (1972).

The terminal velocity v (m/s) of an ice crystal of maximum dimension, L, (μm) is given by

$$v = a_v L^{b_v}, \tag{3.15}$$

where the constants a_v and b_v are dependent on the ice crystal habit and size as given in Starr and Cox (1985). These coefficients were derived at an ambient pressure of 400 mb. For an ice crystal at a given pressure p, Beard and Pruppacher (1969)

have suggested that its terminal velocity may be expressed by

$$v(p) = v(p_*)(p_*/p)^{1/3}, \tag{3.16}$$

where p_* denotes a reference pressure level, and $v(p_*)$ is the terminal velocity of a crystal at the reference level. To obtain the terminal velocity at any given pressure, we simply apply the pressure adjustment to the expression in eq. (3.15).

3.2.7. Downward ice flux. The ice crystal size distribution, ice crystal mass, and terminal velocity are all parameterized in terms of the maximum dimension. Thus, the downward ice flux may be obtained by analytically integrating eq. (3.11), provided that the size of the largest crystal, $L_{\max}$, is known. Since the lower limit, $L_{\min}$, is set to be 20 μm, as stated previously, the upper limit ($L_{\max}$) may be determined from eq. (3.12) as follows: We first obtain $\bar{\rho}\bar{q}_i$ for the nth time step. Subsequently, eqs. (3.13) and (3.14) are substituted into eq. (3.12) to calculate $L_{\max}$. Having determined $L_{\max}$, the downward ice flux can then be computed from eq. (3.11) in the form

$$\bar{V}_T(\bar{\rho}\bar{q}_i) = \frac{a_n a_m a_v}{b_n + b_m + b_v + 1} \times [L_{\max}^{(b_n+b_m+b_v+1)} - L_{\min}^{(b_n+b_m+b_v+1)}]. \tag{3.17}$$

The downward flux is a function of $L_{\max}$, which in turn is a function of cloud IWC.

4. Model performance and verification

4.1. Model input and verification datasets

The atmospheric data generated from the AFGL spectral global model (Yang et al., 1989) analyzed at 1200 GMT 1–4 July 1979, were used as inputs to the cloud model. This period has been chosen because of the availability of cloud and radiation budget data that have been analyzed on a daily basis. The input data contain temperature, specific humidity, and wind fields ($\bar{u}$, $\bar{v}$, $\bar{w}$) at all 12 σ-layers in the atmosphere, plus the surface pressure and geopotential height. These analyses were carried out using a rhomboidal 15 (R15) truncation which corresponds to a horizontal resolution of 38 and 48 grid points in latitude and longitude, respectively. In the vertical, since the GCM-generated input data are available only at the σ-coordinate, it is necessary to perform vertical interpolations to obtain these data in the z-coordinate.

The 3DNEPH cloud data sets have been determined from various satellite, aircraft and ground-based observational sources. Based on 3DNEPH analysis, the global cloud climatologies for January and July 1979 have been processed into appropriate formats for model verification (Koenig et al., 1987). The global distribution of cloud amounts on 1–4 July 1979 is derived from the above cloud climatologies and used as the verification dataset for the cloud cover simulated in the model.

It is important to recognize the limitation of 3DNEPH cloud analysis. A threshold method is employed to process satellite images to determine cloud cover by a threshold temperature. If an observed brightness temperature of a pixel is colder than the threshold temperature, then a cloudy condition is assigned to the pixel. Consequently, the cloud amount tends to be overestimated when the associated surface temperature is low, and underestimated when a temperature inversion is located in the region. This is evident from the fact that 3DNEPH over- and underestimates cloud amounts in the wintertime and summertime polar regions, respectively (Henderson-Sellers, 1986). However, several intercomparisons of the cloud cover between 3DNEPH and the other cloud retrieval techniques have been made (Koenig et al., 1987; Hughes, 1984). The 3DNEPH total cloud cover appears to be reliable, except in the polar regions where all satellite retrieval methodologies tend to fail. Additionally, the surface observational cloud climatology compiled by London (1957) is used as a complementary verification dataset for the polar regions.

The archived ERB flux data tapes for July, 1979, provided by the NASA ERB team (Kyle et al., 1990), are used to validate OLR produced by the model. Since ERB fields are strongly modulated by the radiative effects of clouds, including cloud cover and cloud LWC/IWC, they have been widely used in large-scale cloud model verifications (Slingo, 1987; Smith, 1990). Monthly mean distributions of liquid water have been derived from the Nimbus SMMR observations over the oceans for the period November 1978 to November 1979 (Prabhakara and Short, 1984). The liquid water estimate for July 1979 is applicable to the monthly average over an area approximately 3°

by 5°. The liquid water derived from satellite microwave channels includes vertically integrated amounts of liquid droplets in both clouds and rain. The liquid water verification data are confined to the oceans equatorward of 60° latitude. Over land and ice surfaces, due to the limitation of microwave techniques, there is no climatological liquid water data of global extent for comparisons.

Since there is no ground truth with which to compare, the accuracy of liquid water observations from SMMR is roughly estimated as 100 g/m^2, based on theoretical considerations (Prabhakara et al., 1983). However, by taking monthly averages, this accuracy may be improved to 50 g/m^2 (Prabhakara and Short, 1984).

4.2. Design of the verification and initial data

In the development of any parameterization scheme, the prediction results must be carefully verified to assess its performance. The large scale cloud model was integrated for 96 h with a time step of 30 min from the initial conditions taken at 1200 GMT on 1 July 1979. The wind fields are prescribed from a GCM. It is noted that cloud-radiation feedback to the dynamic structure is not accounted for in this study.

With input of the initial data and wind fields, the cloud model is capable of forecasting large-scale cloud cover and cloud LWC/IWC, which are interactively used in the radiation model. The radiation model computed OLR for comparison with the ERB satellite data. In this study, the interactive radiation computations are undertaken every 3 h, while the calculated heating/cooling rates are input in the cloud model at every time step during those 3 h.

The simulated cloud cover, OLR, cloud LWC and cloud IWC are verified against 3DNEPH cloud cover, ERB data, SMMR results, and in situ observations and other model studies, respectively. However, there are several problems which make the use of satellite observations in model verification not entirely straightforward. For instance, verification datasets such as 3DNEPH and ERB are based on the daily average over local time, while the output of the model simulation is the instantaneous global distribution. In order to allow intercomparisons to be made between the satellite observations and model simulations, we have to average the model predicted fields over local time in order to obtain daily averaged model results.

The analysis data on 12 GMT, 1 July 1979 for temperature and specific humidity are used as initial values to perform a 96-h model simulation. Data for the cloud LWC/IWC are not available for initial values on a global basis. At this point we do not have any physical means to provide the initial cloud LWC/IWC values. For this reason, we have set these values as zero, initially. Unless specified, all of the results including satellite observations and model simulation are averaged over 3–4 July 1979. That is, most of the results shown in this and latter sections are presented as a 2-day average of 3 and 4 July. The 2-day average of the model results circumvents the spin-up problem in the numerical simulations. Due to the limitation of the initial cloud LWC/IWC fields, the results for 1 and 2 July have not been included in the analysis and verification.

4.3. Model results and verification

In Fig. 3a, the model-predicted zonal mean total cloudiness, averaged over 3–4 July, is compared with the corresponding 3DNEPH cloud data. Differences between the two curves are generally within 10% of the total cloud cover except in the tropics, Arctic, and Antarctic areas.

As mentioned in Subsection 4.1, 3DNEPH under- and overestimates cloud covers in Arctic and Antarctic regions, respectively, during the Northern Hemisphere summer. Henderson-Sellers (1986) compared 3DNEPH monthly mean data with London's (1957) cloud climatology which is based on surface cloud observations. Since London's cloud climatology was compiled only for the Northern Hemisphere, the comparison is confined to the Northern Hemisphere. London's cloud climatology shows about 70% of total cloudiness in the summertime Arctic region and 40% in the wintertime. The 70% of total cloudiness in the Arctic is close to our model prediction in the area. This explains the differences between the predicted and 3DNEPH cloud cover in the Arctic and Antarctic regions.

The observed large cloudiness in the tropics is largely caused by tropical anvils, which originate from convective clouds. Since the present large-scale cloud model has been developed primarily for stratiform clouds, the simulated cloud cover in the tropics is underestimated, as is evident in Fig. 3a. Another shortcoming in the simulated cloud cover is the overestimation of cloud cover

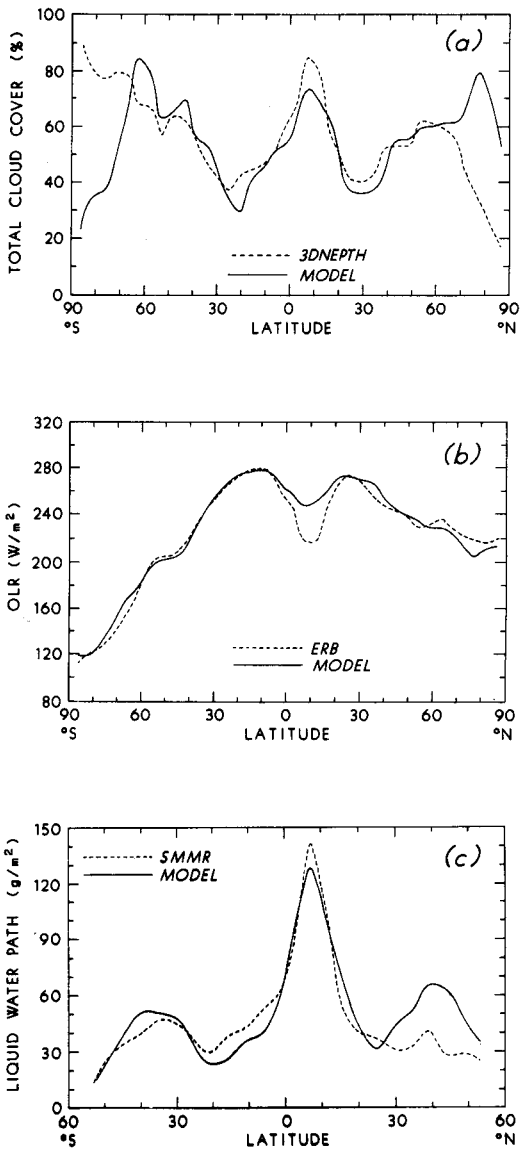

Fig. 3. (a) Comparison of zonal-mean total cloudiness between 3DNEPH and model simulated results averaged over the time period, 3–4 July 1979; (b) Comparison of the zonally averaged OLR computed from the model and derived from ERB data. The model results and ERB data are averaged over the time period, 3–4 July 1979; (c) Comparison of the zonal mean LWP in the simulation and from SMMR data. The SMMR results are taken from Prabhakara and Short (1984) for the monthly average of June 1979. Only the LWPs that are zonally averaged over the oceans are shown in the figure for both simulation and SMMR data.

near 60°S, where the absorbed solar radiation becomes smaller. As a result, strong radiative cooling is produced at the top of middle clouds, leading to a large increase of total cloudiness in the region. It appears that an improvement could be made if a dynamic instability feedback were allowed in the simulation. The simulated small cloud cover located at the subtropic highs in both hemispheres is realistic. Large cloudiness in the tropics is also predicted, although the 3DNEPH cloud data suggests that the predicted cloud cover is underestimated.

Fig. 3b reveals good agreement in OLR between the model simulation and ERB observation, with differences generally less than 10 W/m^2, except in the tropics. The OLR in the tropics predicted from the model is 30 W/m^2 higher than that analyzed from the ERB data. This overestimation of OLR may be explained by the following two factors. First, the altitude of high clouds defined in the model is usually lower than the actual height of tropical anvils. Second, the simulated cloud cover in the tropics is underestimated. Both curves in Fig. 3b indicate two maxima located in the subtropics in both hemispheres with a minimum in the tropics. These two well-defined OLR maxima are associated with the subtropical highs, where small cloudiness coupled with high temperature produces large OLR. The minimum OLR in the tropics is related to the ITCZ region, where thick high clouds are abundant.

Data on cloud LWP are very limited. There are no observational LWP data on a daily basis with which to compare, nor are the zonal averaged values of LWP available for July of 1979. Since the time domain in this study is the very beginning of July, we have compared the predicted zonal mean LWP with the monthly averaged zonal mean data analyzed from SMMR for June, 1979. Fig. 3c shows the zonal mean LWP from model simulations and from SMMR measurements taken from Prabhakara and Short (1984). The zonally averaged LWPs over the oceans are shown in the figure. The zonal mean simulated cloud LWPs compare quite well with SMMR observations. Differences between the two are within 50 g/m^2 which is the uncertainty of SMMR data suggested by Prabhakara and Short.

The maximum LWP that occurs in the tropics is related to the ITCZ. The two well-defined local LWP maxima at mid-latitudes in both

hemispheres are associated with storm tracks. The minimum LWP is found in regions of subtropical highs with prevailing downward motions. The SMMR data show maximum values of about 140, 47, and 40 g/m^2 in the tropics and mid-latitudes, respectively. The corresponding values obtained from simulation are 130, 53, and 65 g/m^2, respectively. The ratio of maximum oberved LWP in the tropics to that in the middle latitude is about 3 to 1. This ratio is about 2 to 1 based on the model simulation. This difference indicates that the model underestimates the cloud LWP in the tropics, where a significant amount of LWP observed by the SMMR is associated with convective clouds, which are not simulated in the present model. The simulated LWPs are larger than the observed values in the midlatitudes of the Northern Hemisphere. However, the differences are all within observational uncertainty.

We have also compared the predicted and observed cloud cover, OLR and LWP, in terms of the horizontal cross-sections to demonstrate the geographical distribution of cloud fields. Below is a brief discussion of these comparisons.

The major distinctive features of the geographical distribution of cloud cover in the observation and simulation include the following. First, a pronounced bright band of cloudiness extends along the ITCZ from 150°W to 90°E. Although the ITCZ cloud band is less pronounced in the simulation, the model reasonably predicts the bright cloud bands extending from the central Pacific to the central Atlantic, and into central Africa. Second, areas of small cloudiness associated with subtropical highs occur both north and south of the ITCZ and are clearly identified in both the observation and the simulation. The oceanic subtropical highs in the Atlantic and Pacific Oceans are also evident from the presence of small cloudiness over the regions. Third, in both the simulation and the observation, cloud bands are found over the east coast of South America, the southern and northern Pacific, and the Greenland Sea. The cloudiness over the east coast of North America is larger in the simulation than in the observation. Finally, the under- and overestimation of cloud cover is shown in the 3DNEPH data in the Arctic and Antarctic regions, respectively, for the Northern Hemisphere summer.

There are two distinct features on the OLR patterns. First, the well defined ITCZ and monsoon circulation are characterized by relatively small values of OLR. They are located over the equatorial western and eastern Pacific, the Atlantic and central Africa, as well as the monsoon area over India and Asia. The cloudiness in these regions is underestimated in the simulation. As a result, the OLR values in these regions are overestimated by the model. Second, the large values of OLR are associated with the subtropical highs located to the south and north of the ITCZ, due to the small cloudiness in the areas. Small OLR values are also evident in the mid-latitude storm tracks in the Northern Hemisphere. The simulated values of OLR in the Greenland Sea are smaller than observed values.

With respect to the geographical distribution of LWP, we have used for comparison the observed data taken from Prabhakara and Short (1984) in terms of the monthly averaged map for July 1979. A large amount of liquid water is shown in the ITCZ. However, in the subtropical highs of both hemispheres, liquid water is small. In the southern Pacific, the model simulates large LWPs, which are also evident in the observed values. In both the simulation and the observation, abundant liquid water is found over the Indian Ocean, and southeast and northeast Asia. In addition, the well-defined observed local LWP maxima near the east coasts of North, Central, and South America are well simulated by the model. The large amount of liquid water associated with the mid-latitude storm tracks near 50°S(N)–60°S(N) is not shown in the SMMR observation because the sea surfaces are largely covered by ice. In addition, the model simulates large amounts of liquid water over land in Central America, central Africa, India and southeast China. These results are not reported by the SMMR observation because of the inability of the microwave technique to function over land.

Since observed cloud IWC has not been available on the global scale, we qualitatively compare the model-predicted cloud IWC with values derived from aircraft measured data in cirrus, as well as with other model results. Based on aircraft measured data in mid-latitude cirrus over the United States, Heymsfield and Platt (1984) have derived the ice crystal size distribution and IWC as functions of temperature. Averaged cloud IWC varies from 0.001 g/m^3 at temperatures below −40°C to about 0.02 g/m^3 above this temperature. Similar cloud IWC values have also been simul-

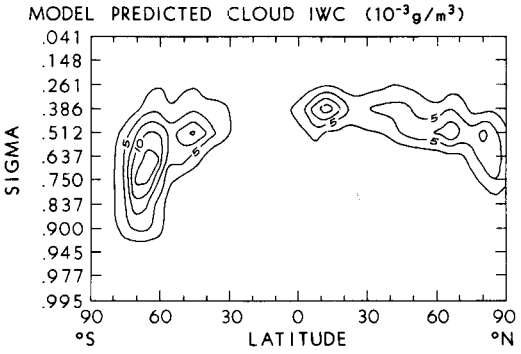

Fig. 4. The model simulations for zonal-mean cloud IWC with a contour interval of 2.5×10^{-3} g/m^3.

ated from a cirrus cloud model by Starr and Cox (1985). The simulated cloud IWC, averaged over 3–4 July 1979, is shown in Fig. 4. The magnitude of the predicted cloud IWC is on the order of 0.01 g/m^3, which is consistent with the other model studies and aircraft observed values in mid-latitude cirrus clouds.

The maxima cloud IWC are located along a temperature of about −15°C, at which the maximum rate of Bergeron-Findeisen's process occurs. The simulated cloud IWC decreases from about 0.01 g/m^3 near −15°C to 0.001 g/m^3 at temperatures below −40°C. The variations of cloud IWC with respect to the temperature obtained from the model are similar to those suggested by Heymsfield and Platt (1984). It is noted that the simulated cloud ice vanishes at temperatures warmer than the melting point, because the melting process converts ice crystals into water droplets. The simulated cloud IWC appears to depend more on temperature than on vertical velocity, which is most significant in the condensation process. The latitudinal distribution of cloud IWC appears to be realistic. In the wintertime Antarctic area, all clouds contain ice, while in the summertime Arctic region, only middle and high clouds are ice clouds. In the tropics, high clouds are largely composed of ice crystals.

5. The role of radiative heating and ice phase processes in cloud formation

In order to examine the effects of radiative heating fields and ice phase microphysics on the large-scale cloud simulations, a set of numerical experiments has been carried out with and without the inclusion of radiative heating and ice phase processes. Below is a brief description of the experimental runs:

- CTRL: Control run which includes both radiation and ice-phase processes.
- EXP1: As in CTRL, but without radiative heating.
- EXP2: As in CTRL, but without the ice-phase processes.

All of the control and experimental runs have the same initial conditions and wind fields. The results are averaged over the same period, allowing intercomparisons to be made between the control and experimental runs.

5.1. Control run

The control run is identical to the experiment described in Subsection 4.2. In that section, the computational results were illustrated in terms of the horizontal cross section. In this section, these results are shown in terms of the meridional cross section so that the vertical structure of cloud fields can be easily identified.

Figs. 5a and 5b show the zonally averaged cloud cover and cloud LWC predicted from the model CTRL. Cloud IWC predicted from CTRL has been shown in Fig. 4. Three cloud cover maxima are seen in the tropics and in the mid-high latitudes of both hemispheres. These maxima are due to large upward motions in these regions. Minima cloud covers occur in the regions of subtropical highs, which are directly related to downward motions. Because of the strong sinking motion of the Southern Hemisphere Hadley cell, cloud cover in the subtropical high of the Southern Hemisphere is smaller than that in the Northern Hemisphere counterpart.

The pattern of simulated cloud LWC in Fig. 5b is consistent with that illustrated in Fig. 5a. The three cloud LWC maxima, located in the tropics and mid-latitude storm tracks, correspond to large cloudiness in these regions. The cloud LWC minima associated with the subtropical highs are due to the prevailing downward motions in the regions. In the vertical, large cloud LWCs are associated with low and middle clouds. The maximum cloud LWC is located in the tropics, and two local maxima exist in mid-latitudes.

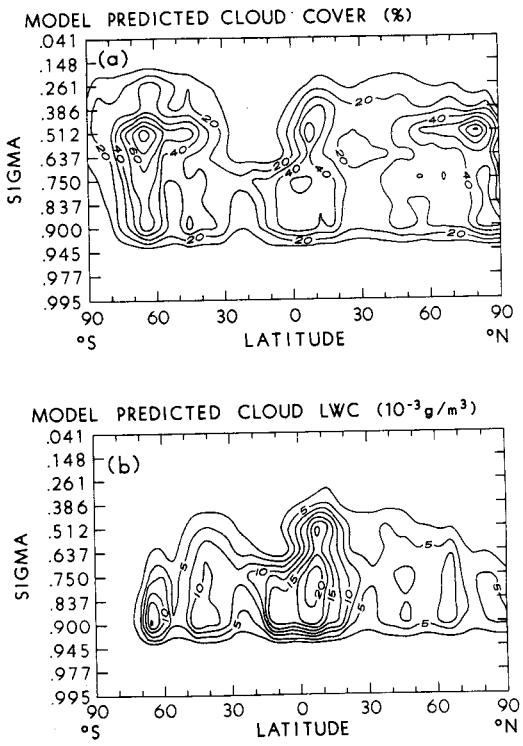

Fig. 5. The model predicted zonal mean fields of (a) cloud cover, and (b) cloud LWC. The model results are averaged over the time period, 3–4 July 1979.

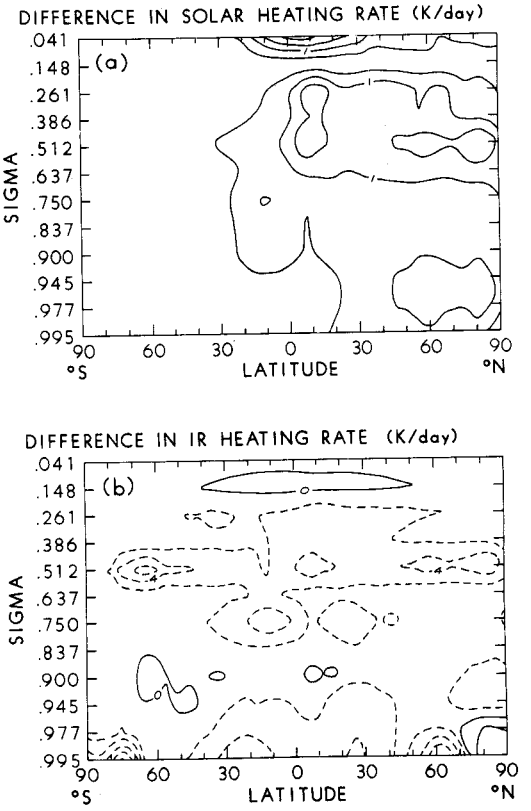

Fig. 6. Zonally averaged differences in (a) solar and (b) IR radiative heating rates. The differences are obtained by subtracting the results in EXP1 from those in CTRL. The contour intervals for solar and IR heating rates are 0.5 and 2 K/day, respectively.

5.2. *Experiment on inclusion of radiative heating*

Figs. 6–8 show the results from the experiments with and without the inclusion of radiative heating. These results are expressed in terms of the differences between two experiments (CTRL–EXP1).

Solar heating rate differences are illustrated in Fig. 6a. Solar radiation heats the atmosphere. As would be expected, the solar heating rates in July of the Northern Hemisphere are much larger than those of the Southern Hemisphere counterpart. There is no solar radiation within the Antarctic Circle because the sun does not rise above the horizon in this region during July. Two solar heating maxima with values of ~ 2 K/day are located at the tops of middle clouds in the Northern Hemisphere. Large solar heating rates within the Arctic Circle are due to long solar days. Large solar heating rates in the tropics are related to small solar zenith angles during the daytime. The large solar heating located in the upper atmosphere is associated with strong ozone absorption.

Fig. 6b shows the IR heating rate differences. The most distinct feature in this figure is the strong IR cooling rates that occur at the middle cloud tops. This is because high clouds are considered to be nonblack in radiation calculations, while middle clouds are assumed to be blackbodies. As a result, the upward IR flux emitted by middle clouds is much stronger than the downward flux emitted by high clouds. Consequently, strong IR radiative cooling is generated at the tops of middle clouds.

The inclusion of IR radiative heating basically cools the atmosphere. However, if low cloudiness is sufficiently large to emit strong downward IR fluxes from the cloud base, weak IR heating may be produced beneath the cloud base. This explains the two regions of weak IR heating at the low

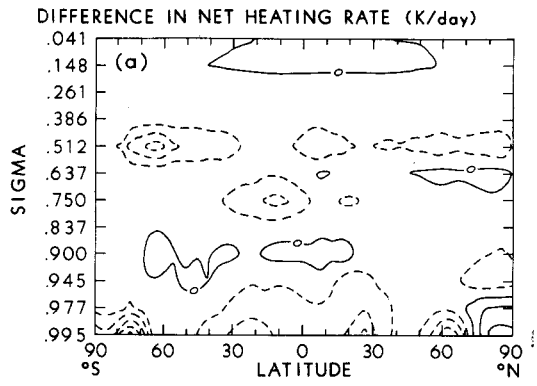

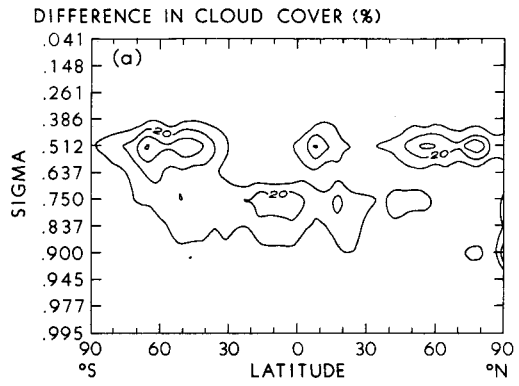

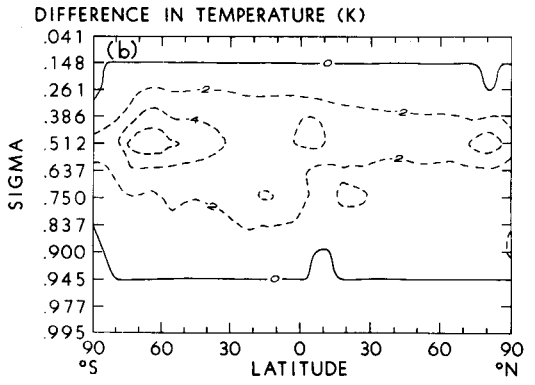

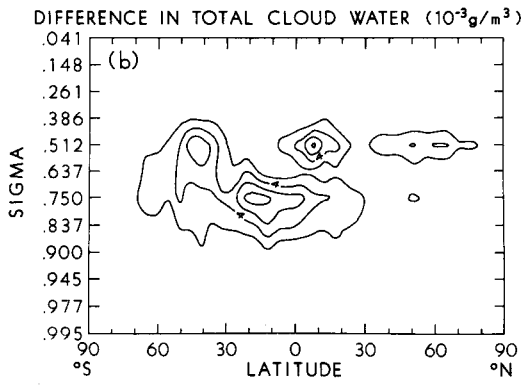

Fig. 7. As in Fig. 6, but for differences in (a) net heating rate and (b) temperature.

Fig. 8. As in Fig. 6, but for differences in (a) cloud cover and (b) total cloud water with contour intervals of 10% and 2×10^{-3} g/m^3, respectively.

cloud bottoms at 60°S and in the tropics. Two other weak IR heating rates, located in the upper tropical atmosphere and in the lower atmosphere in the Arctic, are associated with the areas of high ozone concentration and temperature inversion in the regions, respectively.

Fig. 7a shows net radiative heating rates. The inclusion of radiative processes in the model leads to the decrease of atmospheric temperature. As would be expected, the net radiative heating shows relatively large cooling at middle cloud tops and small cooling at cloud bottoms. However, there are weak heating rates in lower tropical atmospheres and in the Southern Hemisphere due to large low cloud cover over those regions. The strongest radiative cooling at the middle cloud top, located within the Antarctic Circle, is due to the absence of solar radiation in the winter season. Relatively large cooling at the low cloud level within the Arctic area is associated with the temperature inversion in the region, while the large cooling near the surface layers in the equatorial region is due to the contribution of water vapor continuum absorption. It is noted that noticeable net radiative heating is located in the upper atmosphere in the Northern Hemisphere because of the ozone solar absorption in the region. The weak heating at the middle cloud level within the Arctic Circle is due to the absorption of solar radiation during long solar days.

Fig. 7b shows the temperature difference pattern. The inclusion of radiative heating decreases the atmospheric temperature which decreases more significantly for cloudy conditions than clear

sky. The largest temperature reduction occurs at the middle cloud top near 66.5°S, where the sun does not rise much above the horizon in the winter season. Temperature decreases are relatively small in the subtropical regions where small cloud amounts are located. These temperature changes, in turn, initiate all of the changes in the cloud fields such as cloud cover, cloud LWC, and cloud IWC.

Fig. 8a shows differences in cloud cover between the two experiments. The inclusion of radiative heating leads to an increase in cloud cover. Large increases occur at the middle cloud tops, at which large temperature decreases are located. The increases in low cloudiness are relatively small due to small radiative cooling associated with low clouds. However, there are two large increases of low cloud cover. One occurs in the tropics where a large amount of water vapor exists, while the other is in the Arctic area where a strong inversion is located.

Fig. 8b illustrates the differences in total cloud water content, i.e., cloud LWC plus IWC between CTRL and EXP1. Cloud water increases wherever cloud cover increases. As has been mentioned previously, the decrease of cloud temperature by radiative cooling increases the condensational rate and results in the increase of total cloud water. The large increase of cloud water occurs at the tops of middle and low clouds in the tropics, where strong radiative cooling is located.

5.3. *Experiment on ice phase processes*

Figs. 9a and 9b show the results from the experiments with and without the inclusion of ice-phase processes. The differences in temperature and cloud cover due to the inclusion of ice-phase processes are insignificant. Figure 9a illustrates the differences in cloud LWC between the cases with and without the inclusion of ice-phase processes. This figure shows little change in cloud LWC in the tropical low and middle clouds that contain primarily water droplets. Marked reductions of cloud LWC with ice processes included occur in low, middle, and high clouds within the Antarctic Circle, high clouds in the tropics, and middle and high clouds within the Arctic Circle. In these regions clouds are largely composed of ice crystals, which deplete the cloud LWC by virtue of Bergeron-Findeisen's process. Since there is no cloud IWC in EXP2, the differences in cloud IWC are identical to cloud IWC shown in CTRL (see Fig. 4).

Fig. 9b shows the differences in total cloud water content. The increases of total cloud water when the ice phase is included indicate that the increase of ice crystals in clouds is larger than the reduction of cloud LWC. It follows that ice clouds in these regions are not entirely controlled by Bergeron-Findeisen's process.

In order to further examine the relationship between autoconversion and Bergeron-Findeisen's process on cloud formation, we have undertaken two more experimental runs with the autoconversion rate of $c_0 = 10^{-4}\ s^{-1}$, which is five times smaller than what was used in the CTRL. A smaller autoconversion rate leads to the production of more cloud LWC, which in turn generates

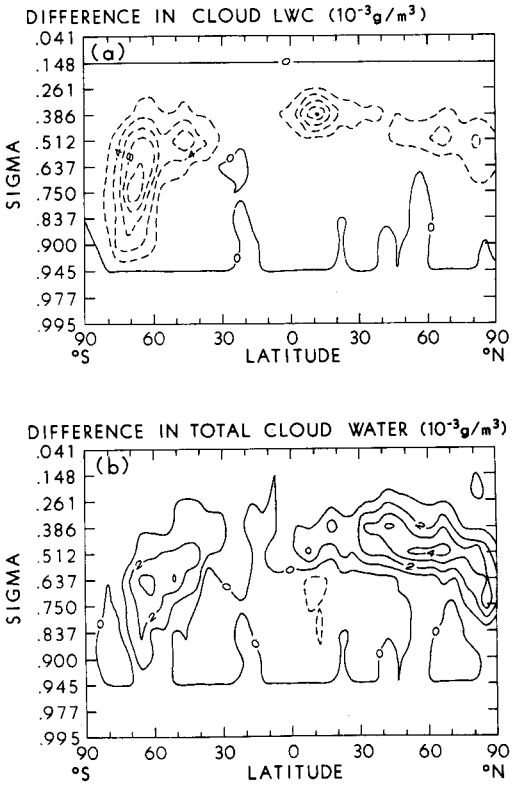

Fig. 9. Zonally averaged differences in (a) cloud LWC and (b) total cloud water. The differences are obtained by subtracting the results in EXP2 from those in CTRL. The contour intervals for cloud LWC and total cloud water are 2×10^{-3} g/m^3 and 10^{-3} g/m^3, respectively.

more cloud IWC through Bergeron-Findeisen's process. In the following two experimental runs, the first run is the same as CTRL with the smaller value of the autoconversion rate, i.e., $c_0 = 10^{-4}$; the second run is the same as the first run but without the ice phase processes.

Fig. 10a shows a pattern very similar to that in Fig. 9a. Due to the smaller value of the autoconversion rate, the differences in cloud LWC are about five times larger in Fig. 10a than they are in Fig. 9a. The large differences in cloud LWC indicate that a strong Bergeron-Findeisen process takes place when there is more cloud LWC. However, the values of cloud IWC in Fig. 10b are close to those in Fig. 4, even though Bergeron-Findeisen's process is much stronger in the former than in the latter. This indicates that the downward ice flux is larger in the former than in the latter.

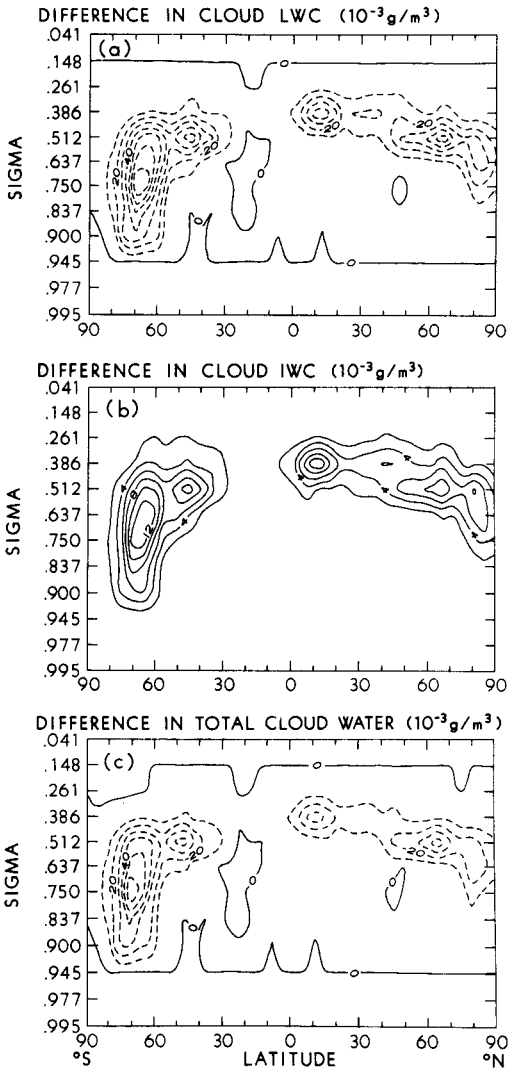

Fig. 10. Zonally averaged differences in (a) cloud LWC, (b) cloud IWC, and (c) total cloud water. The differences are obtained by subtracting the results without ice phase from those with ice phase in the case of a small autoconversion rate. The contour intervals for cloud IWC and cloud LWC and total cloud water are 2×10^{-3} g/m^3 and 10^{-2} g/m^3, respectively.

Fig. 10c shows the differences in total cloud water content for the smaller c_0. The total cloud water content decreases in the region where ice clouds are present. The reduction of the total cloud water content is mainly controlled either by autoconversion that converts cloud LWC into precipitation or by gravitational settling that removes ice crystals from the cloud layer. The decrease of total cloud water content when the ice phase processes are included indicates that gravitational settling is an efficient mechanism for reducing the cloud IWC.

6. Conclusions

A time-dependent, three-dimensional, large-scale cloud-moisture model has been developed for the prediction of temperature, cloud cover, cloud LWC, cloud IWC, and precipitation. The wind fields are prescribed using the results from a GCM. The detailed cloud dynamic processes such as top-down turbulence and entrainment are not considered in this large-scale cloud study. Partial cloudiness is allowed to form when the large-scale relative humidity is less than 100%. The cloud microphysical processes simulated in the model include both liquid and ice phases, which are physically included for the first time in a large-scale cloud model to simulate cirrus clouds.

A 96-h model simulation, with the initial conditions taken at 1200 GMT on 1 July 1979 has been carried out to assess the performance of the large-scale cloud model. The comparisons between the model simulation and the satellite observations indicate the large-scale cloud model is capable of realistically simulating zonal means and geographical distributions of cloud fields, including cloud cover, OLR and net solar flux at TOA,

and cloud LWC. Differences in the zonal mean total cloud cover between the simulation and the 3DNEPH data are generally within 10%. Generally, the simulated zonal mean OLRs are within 10 W/m^2 of the ERB results. The zonal mean values of simulated cloud LWP compare quite well with the SMMR observations, with differences being less than 50 g/m^2, which is the uncertainty of the SMMR data. However, the model underestimates cloud cover and cloud LWC and overestimates the OLR in the tropics, where clouds are predominantly convective types. Convective clouds were not simulated in this model. In the geographical distributions of cloud fields, the large-scale cloud model has simulated the large cloud bands in the ITCZ, monsoon areas, Southern Pacific Convergence Zone, and the mid-latitude storm tracks, although the ITCZ cloud band is less pronounced in the simulation. At the subtropical highs, areas of small cloudiness over southern and northern Africa, and North and South America are clearly identified in both of the observations and the model simulation. The magnitude of the cloud IWC in the simulation is about 0.01 g/m^3, which is consistent with the aircraft measurements in cirrus clouds, as well as with other model results. The simulated cloud IWC appears to depend more on temperature than on vertical velocity, which is critical to the condensational process.

The model-simulated cloud fields are strongly linked to large-scale circulations. Inspecting the model-predicted cloud fields, such as cloud cover, OLR, and cloud LWC, we find that these cloud properties are closely related to one another. Large amounts of cloud cover coincide with abundant cloud LWC, which generates large precipitation rates by virtue of the autoconversion process simulated in the model. In summary, the atmospheric moisture and cloud fields are linked together by the cloud microphysical processes simulated in the cloud model. More importantly, the moisture, cloud fields and earth's radiation budget are physically related to large-scale thermal and dynamical structures, such as temperature and vertical velocity.

Sensitivity studies have been performed to examine the effects of radiative heating fields and ice-phase cloud microphysics on large-scale cloud formation. The inclusion of radiative processes in the cloud formation model significantly decreases the cloud temperature, with the strongest cooling occurring at the middle cloud top. However, there may be weak heating located in a low cloud if cloud cover is sufficiently large to produce a strong downward flux. The decrease of temperature by radiative cooling increases the atmospheric relative humidity and condensation in clouds. As a result, cloud cover and total cloud water, including cloud LWC and IWC, increase due to the inclusion of radiative processes.

The inclusion of ice-phase processes has a greater effect on the cloud LWC and IWC than on the temperature and cloud cover fields. If the cloud LWC is large enough to undertake an effective Bergeron-Findeisen process, the total cloud water content decreases, with large decreases located at the regions where the presence of ice clouds is most pronounced. The reduction of the total cloud water content is mainly controlled either by autoconversion, which converts cloud LWC into precipitation, or by gravitational settling, which removes ice crystals from the cloud layer. The decrease of total cloud water content when the ice-phase processes are included indicates that gravitational settling is an efficient mechanism for reducing the cloud IWC.

7. Acknowledgments

The research work contained in this paper has been supported by the Air Force Office of Scientific Research Grant AFOSR-91-0039. We thank Professor H. Sundqvist for helpful comments on the paper.

REFERENCES

Beard, K. V. and Pruppacher, H. R. 1969. A determination of the terminal velocity and drag of small water drops by means of a wind tunnel. *J. Atmos. Sci. 26*, 1066–1072.

Hansen, J., Russell, G., Rind, D., Stone, P., Lacis, A., Lebedeff, S., Ruedy, R. and Travis, L. 1983. Efficient three-dimensional global models for climate studies: Models I and II. *Mon. Wea. Rev. 111*, 609–662.

Henderson-Sellers, A. 1986. Layered cloud amounts for January and July, 1979 from 3-D Nephanalysis. *J. Clim. Appl. Meteor. 25*, 118–132.

Heymsfield, A. J. 1972. Ice crystal terminal velocities. *J. Atmos. Sci. 29*, 1348–1357.

Heymsfield, A. J. 1977. Precipitation development in stratiform ice clouds: A microphysical and dynamical study. *J. Atmos. Sci. 34*, 367–381.

Heymsfield, A. J. and Platt, C. M. R. 1984. A parameterization of the particle size spectrum of ice clouds in terms of the ambient temperature and the ice water content. *J. Atmos. Sci. 41*, 846–856.

Heymsfield, A. J. and Donner, L. J. 1990. A scheme for parametering ice-cloud water content in general circulation models. *J. Atmos. Sci. 47*, 1865–1877.

Hughes, N. A. 1984. Global cloud climatologies. A historical review. *J. Clim. Appl. Meteor. 23*, 724–751.

Kessler, E. 1969. On the distribution and continuity of water substance in atmospheric circulations. *Meteor. Monogr.* no. 10, American Meteorological Society, Boston, 84 pp.

Koenig, L. R. 1971. Numerical modeling of ice deposition. *J. Atmos. Sci. 28*, 226–237.

Koenig, L. R. and Murray, F. 1976. Ice-bearing cumulus cloud evolution: Numerical simulation and general comparison against observations. *J. Appl. Meteor. 15*, 747–762.

Koenig, G., Liou, K. N. and Griffin, M. 1987. An investigation of cloud radiation interactions using three-dimensional nephanalysis and earth radiation budget data bases. *J. Geophys. Res. 92*, 5540–5554.

Kyle, H. L., Hucek, R. R., Groveman, B. and Frey, R. 1990. *Nimbus 7 ERB narrow field of view: earth radiation budget projects. User's guide.* Goddard Space Flight Center, Greenbelt, MD.

Liou, K. N. 1986. Influence of cirrus clouds on weather and climate processes: A global perspective. *Mon. Wea. Rev. 114*, 1167–1199.

Liou, K. N. and Wittman, G. D. 1979. Parameterization of the radiative properties of clouds. *J. Atmos. Sci. 36*, 1261–1273.

Liou, K. N. and Ou, S. C. 1981. Parameterization of infrared radiative transfer in cloudy atmospheres. *J. Atmos. Sci. 38*, 2707–2716.

Liou, K. N. and Ou, S. C. 1983. Theory of equilibrium temperatures in radiative-turbulent atmospheres. *J. Atmos. Sci. 40*, 214–229.

Liou, K. N. and Zheng, Q. 1984. A numerical experiment on the interactions of radiation, clouds and dynamic processes in a general circulation model. *J. Atmos. Sci. 41*, 1513–1535.

London, J. 1957. A study of the atmospheric heat balance. AFCRC-TR-57-287, College of Engineering, New York University, N.Y.

Mason, B. J. 1971. *The Physics of Clouds.* 2nd Edition, Clarendon Press, 671 pp.

Mitchell, J. F. B., Senior, C. A. and Ingram, W. J. 1989. CO_2 and climate: A missing feedback? *Nature 341*, 132–134.

Ou, S. C. and Liou, K. N. 1983. Parameterization of carbon dioxide 15 μm absorption and emission. *J. Geophys. Res. 88*, 5203–5207.

Ou, S. C. and Liou, K. N. 1988. Development of radiation and cloud parameterization programs for AFGL global models. Scientific Report, Air Force Geophysics Laboratory, AFGL-TR-88-0018, 88 pp.

Prabhakara, C. and Short, D. A. 1984. Nimbus-7 SMMR derived seasonal variations in the water vapor, liquid water and surface winds over the global oceans. *NASA Technical Memorandum 86080*, Goddard Space Flight Center, Greenbelt, Maryland, U.S.A.

Prabhakara, C., Wang, I., Chang, A. T. C. and Gloersen, P. 1983. A statistical examination of Nimbus 7 SMMR data and remote sensing of sea surface temperature, liquid water content in the atmosphere and surface wind speed. *J. Clim. Appl. Meteor. 22*, 2033–2037.

Ramanathan, V., Pitcher, E. J., Malone, R. C. and Blackmon, M. L. 1983. The response of a spectral general circulation model to refinements in radiative processes. *J. Atmos. Sci. 40*, 605–630.

Roeckner, E. 1988. Cloud-radiation feedbacks in a climate model. *Atmos. Res. 21*, 293–303.

Slingo, J. M. 1987. The development and verification of a cloud prediction scheme for the ECMWF model. *Quart. J. Roy. Meteor. Soc. 113*, 899–927.

Slingo, A. and Slingo, J. M. 1988. The response of a general circulation model to cloud longwave radiative forcing. I: Introduction and initial experiments. *Quart. J. Roy. Meteor. Soc. 114*, 1027–1062.

Smagorinsky, J. 1960. On the dynamical prediction of large-scale condensation by numerical methods. *Monograph no. 5*, Amer. Geophys. Union, 71–78.

Smith, R. N. B. 1990. A scheme for predicting layer clouds and their water content in a general circulation model. *Quart. J. Roy. Meteor. Soc. 116*, 435–460.

Starr, D. C. and Cox, S. K. 1985. Cirrus clouds. Part I: A cirrus cloud model. *J. Atmos. Sci. 42*, 2663–2681.

Stephens, G. L. 1978. Radiative properties of extended water clouds. *J. Atmos. Sci. 35*, 2111–2132.

Sundqvist, H. 1978. A parameterization scheme for non-convective condensation including prediction of cloud water content. *Quart. J. Roy. Meteor. Soc. 104*, 677–690.

Sundqvist, H. 1981. Prediction of stratiform clouds: Results from a 5-day forecast with a global model. *Tellus 33*, 242–253.

Sundqvist, H. 1988. Parameterization of condensation and associated clouds in models for weather prediction and general circulation simulation. In: *Physically based modelling and simulation of climate and climatic change.* (ed. M. E. Schlesinger). Reidel, Dordrecht, Part 1, 433–461.

Washington, W. M. and Williamson, D. L. 1977. A description of the NCAR global circulation models. In: *Methods in computational physics, vol. 17. General circulation models of the atmosphere* (ed. J. Chang), pp. 111–172, Academic Press, New York.

Washington, W. M. and Meehl, G. A. 1984. Seasonal

cycle experiment on the climate sensitivity due to a doubling of CO_2 with an atmospheric general circulation model coupled to a simple mixed-layer ocean model. *J. Geophys. Res. 89*, 9475–9503.

Wetherald, R. T. and Manabe, S. 1988. Cloud feedback processes in a general circulation model. *J. Atmos. Sci. 45*, 1397–1415.

Xu, K. M. and Krueger, S. K. 1991. Evaluation of cloudiness parameterizations using a cumulus ensemble model. *Mon. Wea. Rev. 119*, 342–367.

Yang, G. H., Mitchell, K., Norquist, D. and Yee, S. 1989. *Diagnostics for and evaluations of new parameterization schemes for global NWP models.* GL-TR-89-0158. Environmental Research Papers Number 1032, Geophysics Laboratory, Atmospheric Sciences Division, Hanscom AF Base, MA 01731.